Carbon Trends 14 (2024) 100331

Contents lists available at ScienceDirect

Carbon Trends

journal homepage: www.elsevier.com/locate/cartre

Suppression of plasmonic interference in helicity sensitive broadband terahertz detectors

Ilya Mazurenko [a], Dmitriy Vovk [a], Yakov Matyushkin [a,*], Alesia Paddubskaya [b], Maxim Rybin [c], Elena Obraztsova [a,c]

[a] Moscow Institute of Physics and Technology, 9 Institutskiy per., 141701, Dolgoprudny, Moscow Region, Russian Federation
[b] Institute for Nuclear Problems, Belarusian State University, Bobruiskaya str., 11, 220006, Minsk, Belarus
[c] A.M. Prokhorov General Physics Institute, Russian Academy of Sciences, 38 Vavilov Street, 119991, Moscow, Russian Federation

ARTICLE INFO

Keywords:
Graphene
Plasmonic interferometer
Terahertz detection
Helicity-sensitive photoresponse
Field-effect transistor

ABSTRACT

The recently observed helicity-sensitive response, occurring in graphene based field-effect transistors (FETs) is interpreted as a result of the intrinsic phase asymmetry of these devices and interference of plasmons in the FET channel. The graphene-based plasmonic interferometers presented in this work enable the room temperature detection of THz radiation as well as allows us to distinguish between the rotation direction of circular polarized waves. To illustrate the broadband nurture of the observed effects, similar measurements were carried out at both THz and mid-infrared frequencies. The precise control of the carriers type and their concentration throughout the channel length allows us to demonstrate the helicity-sensitive response over a wide range of the gate potentials (from negative to positive values). We experimentally show that the formation of *p*–*n* junction inside the graphene channel leads to additional scattering of excited plasma waves, resulting in the suppression of their interference and consequent reduction of the helicity-sensitive contribution.

Introduction

Plasmonic interferometry in two dimensional materials is a rapidly developing area of both fundamental and applied research [1,2]. Several features facilitate use and observation of plasmonic phenomena in this class of materials. Firstly, the velocity of plasma waves in 2D materials is approximately two orders of magnitude smaller that the speed of light [3]. Hence, the energy of electromagnetic radiation can be confined in a structure much smaller than its wavelength in vacuum or a refractive medium. This property makes surface plasmon interferometers more sensitive to the device geometry and surrounding dielectric media [4]. Secondly, the plasmon phase velocity strongly depends on free carrier concentration and thus can be easily tuned by applying a gate voltage [3].

Graphene is one of the most extensively exploited 2D materials, whose remarkable properties such as high mobility at room temperature [5], thermal conductivity [6], ultra-fast broadband optical response [7,8] and strong mechanical strength open a new area in contemporary solid-state physics and material science [9,10]. Since, the frequency of plasma waves propagated in graphene falls in the THz frequency range, graphene can be used as a “playground” for plasmonic THz applications [11,12]. Furthermore, the slow electron-to-lattice relaxation (1-2 ps) and fast electron-electron scattering (10-100 fs) make graphene a promising material for engineering high-speed optoelectronic THz devices [13–15].

Various methods have been developed for obtaining graphene, including mechanical exfoliation of graphite, decomposition of single-crystal silicon carbide, reduction of graphene oxide, and chemical vapor deposition (CVD) [16]. Despite the high quality of exfoliated graphene, its practical application is limited in terms of sample size and yield, making it unsuitable for the commercial realization of graphene-based devices. In this context, CVD is considered as a promising alternative method to overcome these limitations [17]. However, due to structural defects and chemical contamination introduced during transfer, CVD graphene shows significantly lower carrier mobility than exfoliated graphene, resulting in weakly expressed effects based on graphene plasmonic properties in the CVD-grown structure [18].

Recent results [19–22] indicate that CVD grown graphene transferred onto dielectric surface supports plasmons contributing to graphene interaction with terahertz range radiation. One of the most

* Corresponding author.
E-mail address: ya.matyushkin@gmail.com (Y. Matyushkin).

https://doi.org/10.1016/j.cartre.2024.100331
Received 31 December 2023; Received in revised form 15 February 2024; Accepted 16 February 2024
Available online 27 February 2024

unambiguous demonstrations of plasmon interference in CVD graphene was reported in our previous work [21]. In particular, we showed that the plasma wave interference effect defines the mechanism of THz radiation rectification in graphene-based field-effect transistors (FET) with phase asymmetry. Furthermore, our experimental results demonstrated that the photoresponse of such simple graphene-based devices is sensitive to the radiation helicity suggesting its potential application for the future development of broadband, helicity-sensitive THz detectors and integrated interferometers.

The goal of this work is to investigate the influence of uniformly doping of the graphene channel on the helicity sensitivity of the simple THz devices (graphene-based FET) considered in our previous work. Specifically, within the presented study, similar devices with both single and double gate architectures were fabricated, and their electromagnetic response was investigated in both the THz and mid IR frequency ranges. The double-gated configuration allows us to create non-uniformity at the center of the graphene channel (*p–n* junction), with properties that are easily controllable. We find that the formation of a *p–n* junction leads to the mitigation of the circular effect in contrast to the photovoltaic response induced by mechanisms unrelated to plasmon interference in the graphene channel.

1. Device fabrication and measurements

In our work, the single layer graphene, using as a conducting channel of field-effect transistor (see Fig. 1a and f), was synthesized on Cu foil in a standard tube furnace system. Initially, a copper substrate (25 μm, 99.8%, Alfa-Aesar) was electropolished in 85% concentrated phosphoric acid for 90 s at room temperature (for more details see ref. [23]) and placed in the furnace chamber. The furnace was pumped down, and high purity hydrogen was introduced (the system total pressure was 100 mBar). The Cu foil was annealed at 1000 °C in hydrogen atmosphere for 2 h. After annealing, the chamber was evacuated to 10 mBar and CH_4 was injected to grow graphene. The typical growth time was 2 min. Then, the furnace was cooled down to room temperature.

To transfer the graphene grown from Cu foil to a SiO_2/Si wafer with 500 nm thermal oxide layer and high-resistive Si substrate, polymethylmethacrylate (PMMA) film was spin-coated on surface of the graphene layer. Since the graphene was grown on both sides of the copper substrate, the backside of foil was etched by reactive oxygen plasma (100 W, 15 min). The Cu substrate was dissolved in ammonium persulfate solution for 24 h. The resulting graphene/PMMA structure was rinsed with distilled water, transferred onto a clean SiO_2/Si substrate and dried at 80 °C for 5 min. In order to remove the PMMA layer, the sample was immersed into acetone for 20 min, washed with distilled water and annealed in vacuum at 300 °C for 1 h.

The final device configuration was fabricated using e-beam lithography with PMMA A4 as a resist and oxygen plasma etching. At the first lithography step, two contact pads to graphene were formed using pure Au with a thickness of 30 nm, without an adhesion sub layer (such as titan or chrome). After metal deposition, the graphene channel was patterned using e-beam lithography and reactive ion etching in an oxygen plasma. A typical SEM image of the fabricated graphene-based channel is presented in Fig. 1h. Subsequently, 100 nm thick Al_2O_3 layer, acting as a gate insulator, was deposited via electron beam sputtering. It is worth noting that the Al_2O_3 layer reduces contribution of the major mechanism responsible for the suppression of electron conduction in graphene, namely an oxygen water redox couple-induced electron transfer reaction between graphene and ambient [24], thereby improving the device characteristics. Afterwards, we patterned and formed the top gate electrodes (Ti/Au, 150 nm) using standard sputtering and lift-off techniques. Finally, the tilted bowtie antenna, maintaining phase-asymmetric boundary conditions, was fabricated by optical lithography (see Supporting Information Fig.S2). The choice of the antenna configuration is defined by both its simplicity in fabrication and broadband characteristics.

Within this work, two devices with similar geometry but with different gate configurations were investigated. Device type A (a single-gated device) has a single gate electrode slightly wider than the channel length, ensuring the uniform doping of the graphene. The device configuration is schematically presented in Fig. 1a. Device type B (a double-gated device, Fig. 1f) was fabricated with two split-gates (left and right gate), defining two regions in the graphene channel whose carrier density and type can be controlled by applying voltages. For both fabricated devices, the channel width was 1 μm. The channel length of device type A and device type B were 2.5 and 3 μm, respectively. Optical images of fabricated devices and SEM image of channel area of double-gated device are provided in Supporting Information (Fig.S1).

Before photoresponse measurements, the transport properties of our devices were analyzed at room temperature under a constant source-drain bias of 10 mV. The measured details are explained in the Supporting Information. The two-terminal resistance as a function of the top gate voltage for device type A is presented in Fig. 1c. A full fate sweep consists of both growing and falling sweeps, i.e. from a negative value of $V_g - V_{CNT}$ to a positive value of $V_g - V_{CNT}$ and sweeping back. One can see that the both curves overlap, indicating a good quality of graphene channel and low charge-trapping in $Ti/Au/Al_2O_3$/graphene capacitor [25]. Note that throughout the paper we indicate range of V_g corresponding to the CNP instead of providing its exact value.

The fitting of measured two-terminal resistance data (Fig. 1c) using a simple model recently proposed by Kim et al. [26] allows us to estimate the field-effect carrier mobility μ. Thus, the obtained samples of CVD graphene, after being transferred onto a dielectric substrate, demonstrate a relatively high carrier mobility in range 1000 $cm^2 \cdot V^{-1} \cdot s^{-1}$-3000 $cm^2 \cdot V^{-1} \cdot s^{-1}$, which is typical for CVD graphene at room temperature [20,27]. It should be noted that measured two-terminal resistance curve is asymmetric at two sides of the CNP point. The origin of this asymmetry can be explained by the difference in the scattering cross-section of holes and electrons or may be associated with imbalanced electron-hole injection from graphene electrodes, caused by misalignment of the electrode and channel neutrality point [28].

Fig. 1d plots the resistance map of the double-gated device (Type B) as a function of V_{LG} and V_{RG} (the measurement details are presented in Supporting Information). Four quadrants, corresponding to the four doping constellations in the graphene channel for different combinations of gate voltages, can be identified. When the sign is the same, no *p–n* junction is present in the graphene channel, and only electrons or holes are accumulated in this area (see Fig. 1e). On the other side, when V_{LG} and V_{RG} have the opposite signs, a *p–n* junction, whose size is approximately corresponding to the gap between the two split-gates (gap width $\simeq$ 180 nm) [13], is formed at the center of the graphene channel. One can see the borders of the different areas (dash lines) are not parallel to the V_{LG} and V_{RG} axis due to the cross-talk between two gates [29].

To demonstrate the broadband THz performance of our graphene-based devices, in the context of helicity-sensitivity, the photoresponse was measured at several frequencies. The first experiments were done in the mid-infrared range using a continuous wave quantum cascade laser (QCL) operating at frequency 35 THz (wavelength $\lambda = 8.6$ μm) with an approximate power of 20 mW. The photovoltage was measured using Lock-In SR865 at the modulation frequency, following the standard technique (see Supporting Information for more details). It is worth noting that the beam spot diameter in this setup was about 30 um. Due to the beam size being significantly smaller than the lateral size of our devices, precise control of the device position relative to the incident beam was necessary before each measurement. A Gunn diode was used as a source with a maximum operating power of 10 mW to measure the photoresponse at 0.14 THz (wavelength $\lambda = 2.14$ *mm*). Because the beam cross-section (1-3 mm) was larger than the lateral size of our devices, we can assume that both antennas were uniformly illuminated in this configuration. To study the detector response upon variation of the radiation polarization state, $\lambda/4$-plate of x-cut crystalline quartz

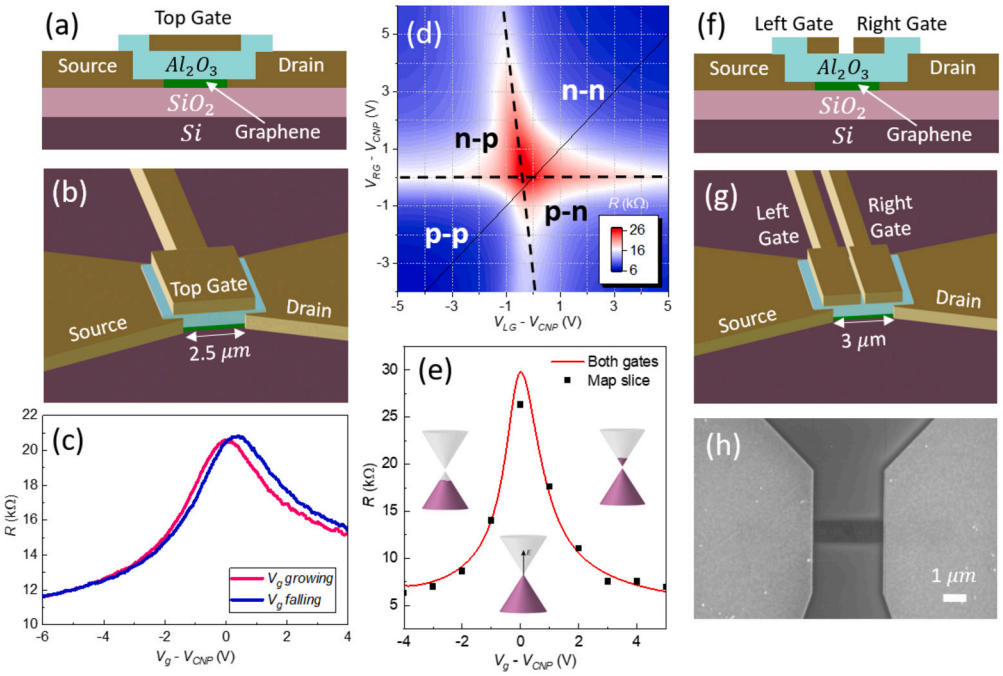

Fig. 1. (a) Single-gated device cross-section scheme. (b) 3D representation of one-gated device. (c) Resistance versus gate voltage of one-gated device. Different colors shows different directions of gate voltage sweeping. (d) Resistance map of double-gated device. Four regions are labeled according to carrier doping in both parts of channel, p-type or n-type, under the left- and right- gated regions, respectively. Filled black line represents the same values of right and left gate. Along this black line both gates acts as one. Inset: resistance color bar in $k\Omega$. (e) Resistance versus gate voltage of double-gated device. Red line obtained when the same voltage was applied to both gates. Black squared dots are extracted from (d) resistance map. Insets: Dirac cones shows how type of quasi particles in graphene channel changes from dots to electrons when Fermi-level cross CNP under gate voltage exposure. (f) Double-gated device cross-section scheme. (g) 3D representation of double-gated device. (h) SEM image of the graphene channel of a double-gated device was obtained during fabrication process.

was used. Both linear and circular polarized light experiments were carried out. In particular, to obtain circular or elliptically polarized beam the quarter-wave plate was rotated by the angle ϕ, between the initial polarization plane and the optical axis of the plate. All experiments were performed at room temperature and for normal incident of polarized THz beam. Different orientations of linearly polarized incident THz beam were obtained by rotation of the additional metal wire polarizer placed between our detector and the quarter-wave plate.

2. Results and discussion

2.1. Single-gated device (Type A)

Figs. 2a and 2c show the photoresponse of the single-gate device (type A) measured at 0.14 and 35 THz, respectively, as a function of the rotation angle of $\lambda/4$-plate and the top gate voltage ($V_g - V_{CNP}$). All presented data were normalized by the incident radiation power collected at the sample position. The comparison of Fig. 2a and Fig. 2b allows us to conclude that the obtained electromagnetic response at different frequencies demonstrates a similar π-periodic angle dependence for almost all values of gate voltage. For clarity, the line cut at the location of the dashed line in Fig. 2a is presented in panel d. Moreover, for right- ($\sigma+$) and left-handed ($\sigma-$) polarizations, i.e., for $\phi = 45°(225°)$ and $135°(315°)$, respectively, the photoresponse has opposite signs without depending on the top gate voltage.

Several different physical principles explaining the electromagnetic response of graphene-based FETs have been reported in recent years [12,15,13,30]. These include the photovoltaic, bolometric, photo thermoelectric, and the plasma-assisted or Dyakonov-Shur effects. However, because the thermoelectric and bolometric effects are caused by heating the graphene electrons, the photoresponse associated with such mechanisms should be insensitive to the local field direction [30] and, in general, cannot explain the helicity-sensitive results considered above.

As it was already demonstrated in ref. [21,31], the observed photoresponse can be well described in the frame of the general model of the interference of two-dimensional plasma waves excited by the source and drain terminals in the transistor channel. Recently, Dyakonov et al. [32–34] shown that the behavior of the electrons in the channel can be well described by the nonlinear hydrodynamic equations:

$$\frac{\partial v}{\partial t} + v\frac{\partial v}{\partial x} + \gamma v = -\frac{e}{m}\frac{\partial U}{\partial x}, \tag{1}$$

$$\frac{\partial U}{\partial t} + \frac{\partial (Uv)}{\partial x} = 0 \tag{2}$$

where v is the velocity of the electric fluid, γ is the electron scattering rate, U is the local value of the gate-to-channel voltage, e and m is the electron charge and effective mass, respectively.

According to our device configuration, the incidence circular polarizer THz radiation couples into the graphene channel by tilted bowtie antenna, whose sleeves are blended by 45°. Due to antenna asymmetry with respect to the direction of the induced current, the boundary conditions for the electron fluid in such transistor channel can be written as follows [35]:

$$U_S = -V_G + U_A \cdot cos(\omega t), \tag{3}$$

$$U_D = -V_G + U_B \cdot cos(\omega t + \nu_{AB}) + V_{PR} \tag{4}$$

where, U_A and U_B are the incidence signal amplitudes near the source and drain terminals, respectively, ω is the round frequency of the incidence THz radiation, V_g is gate-to-channel potential defining the electron concentration in the FET channel. Note, the phase shift between the source and drain potentials (ν_{AB}) depends on the radiation polarization and antenna geometry.

The solution of nonlinear hydrodynamics equations with boundary conditions given by Eq. (3) and (4) allows us to write the general expression for the rectified term V_{PR}:

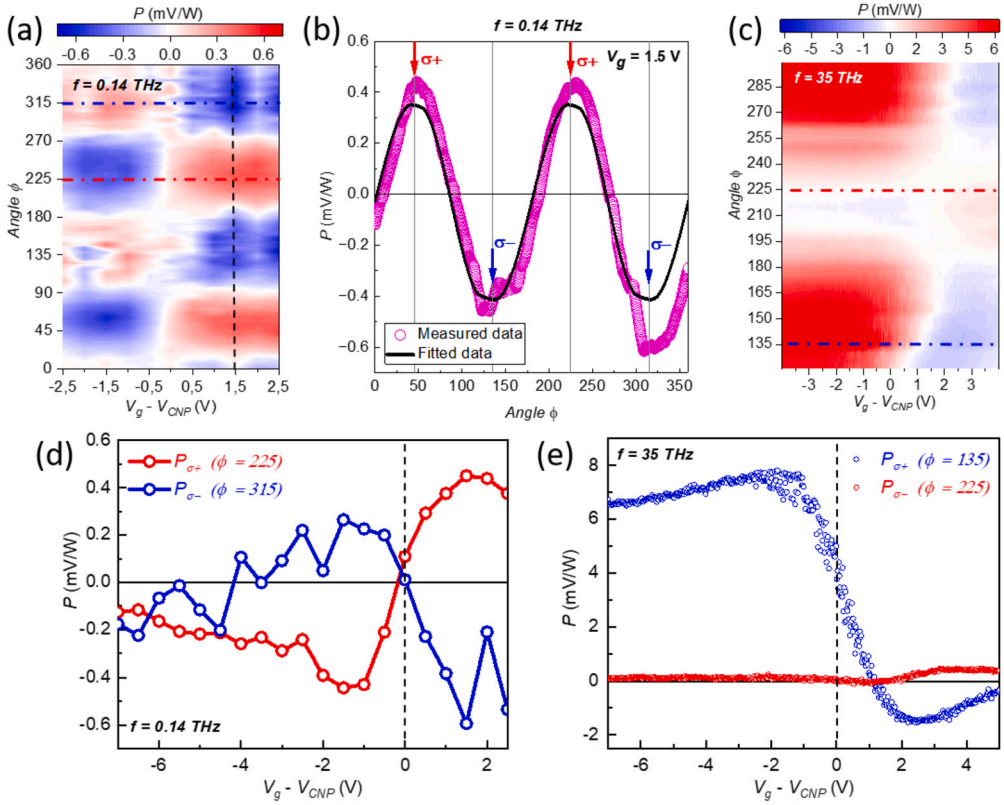

Fig. 2. (a, c) Color map of photoresponse of single-gated device as function of the gate voltage and the rotation angle ϕ of $\lambda/4$-plate measured at 0.14 and 35 THz, respectively. All presented data were normalized by the incident radiation power collected at the sample position. (b) Line cut at the location of the dashed line in panel a, illustrating π-periodicity of photoresponse. The solid line shows the fit of our experimental data by Eq. (1). The following fitting parameters were used: $U_C = 3.8$ μV, $U_{L1} = -0.2$ μV, $U_{L2} = 0.018$ μV and $U_0 = 0.304$ μV. (d, e). Photoresponse as a function of gate voltage, measured for the right ($\sigma+$) and left ($\sigma-$) circularly polarized radiation with frequency 0.14 THz and 35 THz, respectively (horizontal dash-dotted lines in panels a and c).

$$V_{PR} = \alpha<(U_S - U_D)^2> + \beta(<U_S^2> - <U_D^2>) + \delta<U_S \cdot U_D> \quad (5)$$

Here the angular brackets denote the time averaging over the period $2\pi/\omega$. α, β and δ are the parameters determined by dimensionless gate length L, antenna geometry, and channel properties (please see ref. [33]). Note that the last term in Eq. (5) represents the rectification of the incident THz radiation by the plasma wave interference mechanism.

Finally, the dependence of the signal on the rotation angle ϕ of $\lambda/4$-plate can be well-described by the following equation:

$$V_{PR} = U_C sin(2\phi) + U_{L1} sin(4\phi)/2 + U_{L2}[cos(4\phi) + 1]/2 + U_0 \quad (6)$$

with U_C, U_{L1}, U_{L2} and U_0 as the fitting parameters, depending on gate voltage, temperature and frequency. Detailed process of obtaining this equation is contained in our previous work (see equations S7-S18 in ref. [21]). Eq. (6) shows that the total photoresponse is a superposition of (i) the signal proportional to the degree of circular polarization (first term) and (ii) the signal determined by the linear polarization (second and third terms). In other words, the magnitude of the U_C term characterizes the helicity-sensitive response. Fig. 2b shows the fitting results of our experimental data by Eq. (6).

According to Eq. (5) and (6), experimentally, the helicity-sensitive contribution U_C can be estimated by comparing the electromagnetic response measured with right-handed (U_{σ_+}) and left-handed (U_{σ_-}) circularly polarized radiation $U_C = \left(U_{\sigma_+} - U_{\sigma_-}\right)/2$). Figs. 2d and 2e illustrate the results of such measurements for the single-gated device at frequencies 0.14 THz and 35 THz, respectively. The data show that the obtained photoresponse is symmetrical up to sign relative to the CNP. Similar results have been demonstrated in ref. [21]. However, due to additional inhomogeneities in the graphene channel associated with the presented undoping graphene areas (see Fig.1b in reference [21]), the U_C was more pronounced at the positive gate voltage (see Fig.3 in reference [21]), where the channel is electrostatically doped with electrons. One of the principal observations here is that choosing a gate configuration slightly wider than the channel length allows us to demonstrate the helicity-sensitive response for both carrier types. Furthermore, as seen from the experimental data, the interference mechanism dominates at gate voltage close to CNP regardless of the frequency. Such frequency-independent behavior can be explained by the linear dispersion of plasma waves in the graphene channel [36].

2.2. Double-gated devices (Type B)

As mentioned above, the double-gated configuration allows us to create non-uniformity in the graphene channel, whose properties can be controlled by changing V_{LG} and V_{RG}. Similar to device type A, the photoresponse as a function of $\lambda/4$-plate rotation angle and both gate voltages, V_{LG} and V_{RG}, respectively, was measured at 0.14 THz and 35 THz, and the helicity-sensitive term (U_C) was evaluated based on the experimental data as described above. The main results obtained for such device type are illustrated in Fig. 3.

The results clearly indicate that at both frequencies, the relatively strong helicity-sensitive contribution is observed when both parts of graphene channel are n-doped ($\sim 0.4 mV/W$ at 0.14 THz and $\sim 9.1 mV/W$ at 35 THz). However, this contribution is notably lower when both parts are p-doped ($\sim 0.1 mV/W$ at 0.14 THz and $\sim 2.3 mV/W$ at 35 THz). The observed asymmetry in the electromagnetic response of devise type B can be attributed to a small ungated area with a width of around 180 nm located between the two gate electrodes. This finding is in agreement with the results obtained for single-gated device (device type A) and supports one of the conclusions of our previous work [21]. When the V_{LG} and V_{RG} have opposite signs (marked

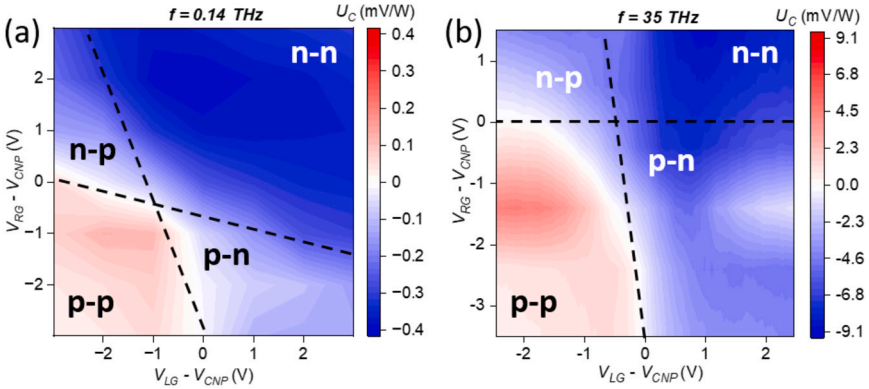

Fig. 3. Color map of the helicity-sensitive response ($U_C = (P_{\sigma^+} - P_{\sigma^-})/2$) of the double-gated device as a function of V_{LG} and V_{RG}, measured at 0.14 and 35 THz, respectively. All presented data were normalized by the incident radiation power collected at the sample position. The dashed lines indicate the CNP position for V_{LG} and V_{RG}. Let us note that panel (a) illustrates the photoresponse obtained for the device with channel length of 2 um and channel width of 5.5 μm, the resistance map of which is presented in Supporting Information (see Fig.4S).

as *n–p* and *p–n* in Fig. 3) the helicity response is weak which can be explained by plasma waves scattering on the obtained *n–p* or *p–n* junction.

Thus, the proper choice between the values of the V_{LG} and V_{RG} potentials allows one to completely suppress or enhance the helicity-sensitive contribution to the total photoresponse of such THz devices. The development of a theoretical model describing the scattering plasmon waves on the *p–n* junction inside the FET channel is outside the scope of this study and we will address this task in our future research.

3. Conclusions

We have demonstrated the broadband nature of the helicity-sensitive response of our graphene-based devices operating at room temperature. The contribution of helicity-dependent detection was interpreted within the framework of the general model of interference of plasma waves propagating in the graphene channel. By comparing the photoresponse of both single-gated and double-gated devices, we experimentally show that the gate design controls the efficiency of such interference effects. We expect that the obtained results are substantial for the future development of novel graphene-based THz devices capable of analyzing both the amplitude and polarization state of THz radiation.

CRediT authorship contribution statement

Ilya Mazurenko: Writing – original draft, Investigation, Conceptualization. **Dmitriy Vovk:** Data curation, Conceptualization. **Yakov Matyushkin:** Writing – review & editing, Visualization, Project administration, Investigation. **Alesia Paddubskaya:** Writing – original draft, Validation, Formal analysis. **Maxim Rybin:** Resources, Data curation. **Elena Obraztsova:** Writing – review & editing, Supervision, Conceptualization.

Declaration of competing interest

The authors declare that they have no known competing financial interests or personal relationships that could have appeared to influence the work reported in this paper.

Data availability

Data will be made available on request.

Acknowledgements

The authors thank Georgy Fedorov for valuable discussions during the preparation of the publication. The reported study was funded by RFBR and BRFBR, project number 20-52-04012. The graphene formation and characterization was supported by project RScF 21-72-20050.

Appendix A. Supplementary material

Supplementary material related to this article can be found online at https://doi.org/10.1016/j.cartre.2024.100331.

References

[1] J. Feng, V.S. Siu, A. Roelke, V. Mehta, S.Y. Rhieu, G.T.R. Palmore, D. Pacifici, Nanoscale plasmonic interferometers for multispectral, high-throughput biochemical sensing, Nano Lett. 12 (2) (2012) 602–609, https://doi.org/10.1021/nl203325s.
[2] Q. Ma, G. Ren, K. Xu, J.Z. Ou, Tunable optical properties of 2d materials and their applications, Adv. Opt. Mater. 9 (2) (Nov. 2020), https://doi.org/10.1002/adom.202001313.
[3] V. Ryzhii, Terahertz plasma waves in gated graphene heterostructures, Jpn. J. Appl. Phys. 45 (9L) (2006) L923, https://doi.org/10.1143/jjap.45.l923.
[4] K.Y.M. Yeung, H. Yoon, W. Andress, K. West, L. Pfeiffer, D. Ham, Two-path solid-state interferometry using ultra-subwavelength two-dimensional plasmonic waves, Appl. Phys. Lett. 102 (2) (Jan. 2013), https://doi.org/10.1063/1.4775668.
[5] A.S. Mayorov, R.V. Gorbachev, S.V. Morozov, L. Britnell, R. Jalil, L.A. Ponomarenko, P. Blake, K.S. Novoselov, K. Watanabe, T. Taniguchi, A.K. Geim, Micrometer-scale ballistic transport in encapsulated graphene at room temperature, Nano Lett. 11 (6) (2011) 2396–2399, https://doi.org/10.1021/nl200758b.
[6] A.A. Balandin, Thermal properties of graphene and nanostructured carbon materials, Nat. Mater. 10 (8) (2011) 569–581, https://doi.org/10.1038/nmat3064.
[7] Z. Sun, T. Hasan, F. Torrisi, D. Popa, G. Privitera, F. Wang, F. Bonaccorso, D.M. Basko, A.C. Ferrari, Graphene mode-locked ultrafast laser, ACS Nano 4 (2) (2010) 803–810, https://doi.org/10.1021/nn901703e.
[8] F. Bonaccorso, Z. Sun, T. Hasan, A.C. Ferrari, Graphene photonics and optoelectronics, Nat. Photonics 4 (9) (2010) 611–622, https://doi.org/10.1038/nphoton.2010.186.
[9] K.S. Novoselov, A.K. Geim, S.V. Morozov, D. Jiang, Y. Zhang, S.V. Dubonos, I.V. Grigorieva, A.A. Firsov, Electric field effect in atomically thin carbon films, Science 306 (5696) (2004) 666–669, https://doi.org/10.1126/science.1102896.
[10] M.S. Vitiello, Nanodevices at terahertz frequency based on 2d materials, J. Phys., Mater. 3 (1) (2019) 014008, https://doi.org/10.1088/2515-7639/ab5843.
[11] A.N. Grigorenko, M. Polini, K.S. Novoselov, Graphene plasmonics, Nat. Photonics 6 (11) (2012) 749–758, https://doi.org/10.1038/nphoton.2012.262.
[12] F.H.L. Koppens, T. Mueller, P. Avouris, A.C. Ferrari, M.S. Vitiello, M. Polini, Photodetectors based on graphene, other two-dimensional materials and hybrid systems, Nat. Nanotechnol. 9 (10) (2014) 780–793, https://doi.org/10.1038/nnano.2014.215.
[13] L. Viti, A.R. Cadore, X. Yang, A. Vorobiev, J.E. Muench, K. Watanabe, T. Taniguchi, J. Stake, A.C. Ferrari, M.S. Vitiello, Thermoelectric graphene photodetectors with sub-nanosecond response times at terahertz frequencies, Nanophotonics 10 (1) (2020) 89–98, https://doi.org/10.1515/nanoph-2020-0255.
[14] L. Viti, D.G. Purdie, A. Lombardo, A.C. Ferrari, M.S. Vitiello, Hbn-encapsulated, graphene-based, room-temperature terahertz receivers, with high speed and low

noise, Nano Lett. 20 (5) (2020) 3169–3177, https://doi.org/10.1021/acs.nanolett.9b05207.
[15] S. Castilla, B. Terrés, M. Autore, L. Viti, J. Li, A.Y. Nikitin, I. Vangelidis, K. Watanabe, T. Taniguchi, E. Lidorikis, M.S. Vitiello, R. Hillenbrand, K.-J. Tielrooij, F.H. Koppens, Fast and sensitive terahertz detection using an antenna-integrated graphene pn junction, Nano Lett. 19 (5) (2019) 2765–2773, https://doi.org/10.1021/acs.nanolett.8b04171.
[16] S. Xu, L. Zhang, B. Wang, R.S. Ruoff, Chemical vapor deposition of graphene on thin-metal films, Cell Rep. Phys. Sci. 2 (3) (2021) 100372, https://doi.org/10.1016/j.xcrp.2021.100372.
[17] J.-Y. Moon, M. Kim, S.-I. Kim, S. Xu, J.-H. Choi, D. Whang, K. Watanabe, T. Taniguchi, D.S. Park, J. Seo, S.H. Cho, S.-K. Son, J.-H. Lee, Layer-engineered large-area exfoliation of graphene, Sci. Adv. 6 (44) (Oct. 2020), https://doi.org/10.1126/sciadv.abc6601.
[18] Z. Zhang, Y. Lee, M.F. Haque, J. Leem, E.Y. Hsieh, S. Nam, Plasmonic sensors based on graphene and graphene hybrid materials, Nano Converg. 9 (1) (Jun. 2022), https://doi.org/10.1186/s40580-022-00319-5.
[19] I.A. Gayduchenko, G.E. Fedorov, M.V. Moskotin, D.I. Yagodkin, S.V. Seliverstov, G.N. Goltsman, A.Y. Kuntsevich, M.G. Rybin, E.D. Obraztsova, V.G. Leiman, M.S. Shur, T. Otsuji, V.I. Ryzhii, Manifestation of plasmonic response in the detection of sub-terahertz radiation by graphene-based devices, Nanotechnology 29 (24) (2018) 245204, https://doi.org/10.1088/1361-6528/aab7a5.
[20] A. Bylinkin, E. Titova, V. Mikheev, E. Zhukova, S. Zhukov, M. Belyanchikov, M. Kashchenko, A. Miakonkikh, D. Svintsov, Tight-binding terahertz plasmons in chemical-vapor-deposited graphene, Phys. Rev. Appl. 11 (5) (May 2019), https://doi.org/10.1103/physrevapplied.11.054017.
[21] Y. Matyushkin, S. Danilov, M. Moskotin, V. Belosevich, N. Kaurova, M. Rybin, E.D. Obraztsova, G. Fedorov, I. Gorbenko, V. Kachorovskii, S. Ganichev, Helicity-sensitive plasmonic terahertz interferometer, Nano Lett. 20 (10) (2020) 7296–7303, https://doi.org/10.1021/acs.nanolett.0c02692.
[22] S. Zanotto, L. Bonatti, M.F. Pantano, V. Mišeikis, G. Speranza, T. Giovannini, C. Coletti, C. Cappelli, A. Tredicucci, A. Toncelli, Strain-induced plasmon confinement in polycrystalline graphene, ACS Photonics 10 (2) (2023) 394–400, https://doi.org/10.1021/acsphotonics.2c01157.
[23] M. Rybin, A. Pereyaslavtsev, T. Vasilieva, V. Myasnikov, I. Sokolov, A. Pavlova, E. Obraztsova, A. Khomich, V. Ralchenko, E. Obraztsova, Efficient nitrogen doping of graphene by plasma treatment, Carbon 96 (2016) 196–202, https://doi.org/10.1016/j.carbon.2015.09.056.
[24] C.G. Kang, Y.G. Lee, S.K. Lee, E. Park, C. Cho, S.K. Lim, H.J. Hwang, B.H. Lee, Mechanism of the effects of low temperature al2o3 passivation on graphene field effect transistors, Carbon 53 (2013) 182–187, https://doi.org/10.1016/j.carbon.2012.10.046.
[25] J.E. Muench, A. Ruocco, M.A. Giambra, V. Miseikis, D. Zhang, J. Wang, H.F.Y. Watson, G.C. Park, S. Akhavan, V. Sorianello, M. Midrio, A. Tomadin, C. Coletti, M. Romagnoli, A.C. Ferrari, I. Goykhman, Waveguide-integrated, plasmonic enhanced graphene photodetectors, Nano Lett. 19 (11) (2019) 7632–7644, https://doi.org/10.1021/acs.nanolett.9b02238.
[26] S. Kim, J. Nah, I. Jo, D. Shahrjerdi, L. Colombo, Z. Yao, E. Tutuc, S.K. Banerjee, Realization of a high mobility dual-gated graphene field-effect transistor with al2o3 dielectric, Appl. Phys. Lett. 94 (6) (Feb. 2009), https://doi.org/10.1063/1.3077021.
[27] M.A. Giambra, V. Mišeikis, S. Pezzini, S. Marconi, A. Montanaro, F. Fabbri, V. Sorianello, A.C. Ferrari, C. Coletti, M. Romagnoli, Wafer-scale integration of graphene-based photonic devices, ACS Nano 15 (2) (2021) 3171–3187, https://doi.org/10.1021/acsnano.0c09758.
[28] D.B. Farmer, R. Golizadeh-Mojarad, V. Perebeinos, Y.-M. Lin, G.S. Tulevski, J.C. Tsang, P. Avouris, Chemical doping and electron-hole conduction asymmetry in graphene devices, Nano Lett. 9 (1) (2009) 388–392, https://doi.org/10.1021/nl803214a.
[29] A.L. Grushina, D.-K. Ki, A.F. Morpurgo, A ballistic pn junction in suspended graphene with split bottom gates, Appl. Phys. Lett. 102 (22) (Jun. 2013), https://doi.org/10.1063/1.4807888.
[30] V. Semkin, D. Mylnikov, E. Titova, S. Zhukov, D. Svintsov, Gate-controlled polarization-resolving mid-infrared detection at metal–graphene junctions, Appl. Phys. Lett. 120 (19) (May 2022), https://doi.org/10.1063/5.0088724.
[31] Y. Matyushkin, S. Danilov, M. Moskotin, G. Fedorov, A. Bochin, I. Gorbenko, V. Kachorovskii, S. Ganichev, Carbon nanotubes for polarization sensitive terahertz plasmonic interferometry, Opt. Express 29 (23) (2021) 37189, https://doi.org/10.1364/oe.435416.
[32] M. Dyakonov, M. Shur, Shallow water analogy for a ballistic field effect transistor: new mechanism of plasma wave generation by dc current, Phys. Rev. Lett. 71 (15) (1993) 2465–2468, https://doi.org/10.1103/physrevlett.71.2465.
[33] M.I. Dyakonov, Generation and detection of terahertz radiation by field effect transistors, C. R. Phys. 11 (7–8) (2010) 413–420, https://doi.org/10.1016/j.crhy.2010.05.003.
[34] K.S. Romanov, M.I. Dyakonov, Theory of helicity-sensitive terahertz radiation detection by field effect transistors, Appl. Phys. Lett. 102 (15) (2013) 153502, https://doi.org/10.1063/1.4801946.
[35] I.V. Gorbenko, V.Y. Kachorovskii, M. Shur, Terahertz plasmonic detector controlled by phase asymmetry, Opt. Express 27 (4) (2019) 4004, https://doi.org/10.1364/oe.27.004004.
[36] I.V. Gorbenko, V.Y. Kachorovskii, M.S. Shur, Plasmonic helicity-driven detector of terahertz radiation, physica status solidi (RRL), Rapid Res. Lett. 13 (3) (Dec. 2018), https://doi.org/10.1002/pssr.201800464.